Transient fields in the input coupling region of optical single-mode waveguides

Werner Klaus[1*] and Walter R. Leeb[2]

[1]National Institute of Information and Communications Technology (NICT),
4-2-1, Nukui-Kitamachi, Koganei, Tokyo 184-8795, Japan
[2]Institute for Communications and Radio-Frequency Engineering, Vienna University of Technology,
Gusshausstrasse 25/389, A-1040 Wien, Austria
[*]Corresponding author: klaus@nict.go.jp

Abstract: We investigate numerically the optical field in the region immediately behind the input facets of dielectric step-index single-mode slab and fiber waveguides. Visualization of the intensity distributions gives insight into the formation of the fundamental mode and of radiation modes. For a more quantitative characterization we determine the amount of optical power and mode purity of the field in core vicinity as a function of propagation distance. The investigation assists in designing and optimizing waveguides being employed as modal filters, e.g. for astronomical interferometers.

References and links

1. B. Mennesson, M. Ollivier, and C. Ruilier, "Use of single-mode waveguides to correct the optical defects of a nulling interferometer," J. Opt. Soc. Am. A **19**, 596-602 (2002).
2. O. Wallner, W. R. Leeb, and R. Flatscher, "Design of spatial and modal filters for nulling interferometry," in *Interferometry for Optical Astronomy II*, Wesley A. Traub, ed., Proc. SPIE **4838**, 668-679 (2003).
3. J. C. Flanagan, D. J. Richardson, M. J. Foster, and I. Bakalski, "Microstructured fibers for broadband wavefront filtering in the mid-IR," Opt. Express **14**, 11773-11786 (2006).
4. C. V. M. Fridlund, "DARWIN – The Infrared Space Interferometry Mission," ESA Bulletin **103**, 20-25 (2000).
5. O. Wallner, *et al*., "Minimum length of a single-mode fiber spatial filter," J. Opt. Soc. Am. A **19,** 2445-2448 (2002).
6. P. Cheben, D. -X. Xu, S. Janz, and A. Densmore, "Subwavelength waveguide grating for mode conversion and light coupling in integrated optics," Opt. Express **14**, 4695-4702 (2006).
7. L, Li, "New formulation of the Fourier modal method for crossed surface-relief gratings," J. Opt. Soc. Am. A **14,** 2758-2767 (1997).
8. A. W. Snyder and J. D. Love, *Optical waveguide theory* (Chapman & Hall, 1983), p. 259 ff.
9. G. Grau and W. Freude, *Optische Nachrichtentechnik* (Springer, 1991), pp. 51.
10. E. Silberstein *et al*., "Use of grating theories in integrated optics," J. Opt. Soc. Am. A **18**, 2865-2875 (2001).
11. C. Zhou and L. Li, "Formulation of the Fourier modal method for symmetric crossed gratings in symmetric mountings," J. Opt. A: Pure Appl. Opt. **6**, 43-50 (2004).

1. Introduction

In a single-mode optical waveguide, the field distribution commonly called fundamental mode constitutes a steady-state solution of Maxwell's equations. Strictly speaking, it exists only if the radiation at the guide's input facet already perfectly matches the mode in both amplitude and phase, or after infinitely long guidance. Yet, relatively short pieces of single-mode fibers may act as highly effective modal filters. A modal filter has to provide a unique amplitude and phase distribution at its output facet, irrelevant of the input field. Modal filters constitute key devices in interferometric instruments where pronounced destructive interference of two or

more input beams is required [1-3]. An example for such an application is ESA's DARWIN mission which aims at the investigation of extra-solar planets [4]. The concept relies on astronomical interferometry and asks for an excessive nulling capability to suppress the star's radiation while analyzing the faint light reflected from a nearby planet.

In a modal filter, the swift convergence of the field distribution towards the one of the fundamental mode is highly desirable. It will depend on waveguide geometry and material properties, and of course on the form of the incident wave. For an efficient design it is essential to understand the formation of the fundamental mode shortly behind the input facet and its dependence on the waveguide parameters. A good design will be characterized by a waveguide length that is as short as possible without sacrificing too much modal filter functionality. One attempt to analytically estimate the minimum length of an ideal fiber waveguide was presented in [5]. That approach, however, could not take into account many of the real-world aspects occurring from the viewpoint of both the input field and the waveguide geometry. Concerning the problem of input coupling, more recently a method was proposed for achieving efficient mode conversion between a fiber and a sub-micrometer waveguide by using a subwavelength grating [6].

Here we present results for the field distribution in the input coupling region of single-mode waveguides as obtained with a rigorous numerical tool based on the Fourier Modal Method [7]. To gain basic insight into the field behavior shortly behind the input facet, we first analyze the computationally easier two-dimensional case, i.e. a slab waveguide. We examine how the intensity distribution near the core reaches the steady-state of the fundamental mode and calculate power flow and coupling efficiency. We further define and calculate the mode purity which serves as a quantitative measure of the conformity of the field with the ideal fundamental mode. In a second step, we examine to a lesser extent the computationally much more extensive three-dimensional fiber waveguide, and in particular look for any fundamental differences in field behavior, power distribution and mode purity compared to the slab waveguide.

The paper is structured as follows: In Section 2 we describe the system model and introduce some definitions required for the proper description of the output field's quality. In Section 3 we outline the numerical method employed. Section 4 is dedicated to the discussions of the numerical results of slab and fiber waveguide. Various input coupling situations and the effect of an input pupil positioned just in front of the waveguide's input facet are investigated. In Section 5 we compare the results obtained for the slab waveguide with those for the fiber waveguide, while Section 6 demonstrates the excellent agreement between numerical results and analytical solutions for some special cases. Finally, in Section 7 we present a summary and conclusions.

2. Waveguide modeling and definitions of characteristics

Figure 1 shows the waveguide model and an idealized optical set-up used to estimate the quality of the mode at the waveguide output. The step-index single-mode waveguide consists of a core with refractive index n_1 and thickness $2a$, and an infinitely thick cladding with index n_2. Both input and output facets are assumed to carry an ideal antireflection coating. A pupil of width D_A may be positioned just in front of the waveguide's input facet to hinder part of the input field from being coupled into the cladding and thus removing undesired field fractions inside the waveguide. Another pupil of width D_B placed immediately behind the waveguide's output facet serves as the exit pupil controlling the size of the field sample to be used for the evaluation of the mode purity.
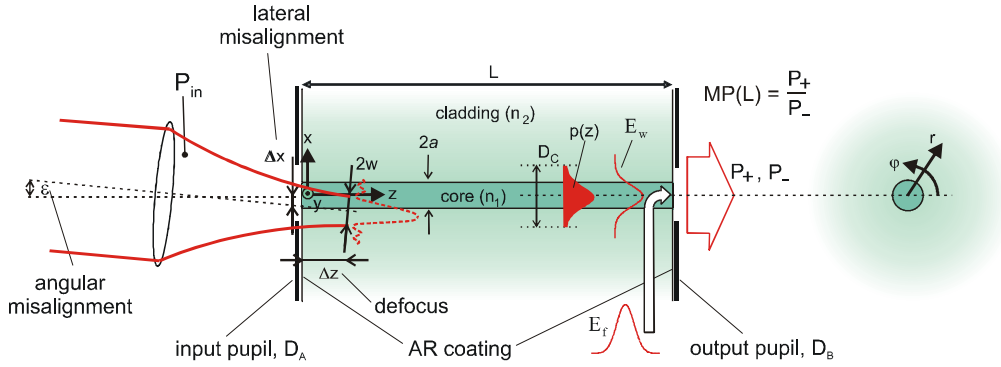
Fig. 1. System model. P_{in} .. input power, $2w$ .. beam width (defined by first zeros in the focal plane), $2a$ .. core width, D_A .. input pupil width, D_B .. output pupil width, D_C .. near-core power width, $p(z)$ .. near-core power, E_W .. waveguide field just before output facet, E_f .. field of fundamental mode. The constructive and destructive superposition of field E_w with the fundamental mode E_f leading to output power P_+ and P_- serves only to illustrate the definition of mode purity MP. The right part shows the cross section in case of a fiber waveguide.

Table 1 lists the waveguide parameters chosen for the numerical calculations presented in Section 4, with λ_0 representing the shortest wavelength under consideration. For both the slab and the fiber, operation at wavelength $\lambda = \lambda_0$ is a few percent below the cut-off of the first higher-order mode. The input pupil is modeled to consist of a metallic layer of thickness λ_0 with index of refraction $n = 0.5 + j10$.

Table 1. Waveguide parameters used for the numerical calculations (Δ .. relative index difference, V .. normalized frequency, V_C .. cut-off frequency). Also given is the input pupil width D_A (if not explicitly set to infinity) and the output pupil width D_B.

	$2a$	n_1	n_2	Δ	V @ λ_0	V @ λ_0/ V_C	D_A	D_B
slab	$4.5\,\lambda_0$	1.50375	1.5	0.25%	1.5004	95.5%	$11\,\lambda_0$	$18\,\lambda_0$
fiber	$4.5\,\lambda_0$	1.50850	1.5	0.56%	2.2607	94.0 %	$8.8\,\lambda_0$	$18\,\lambda_0$

An ideal lens focuses a truncated plane wave to a spot in the focal plane. This plane may be offset from the input plane by a distance Δz ("defocus"). (A positive Δz means that the focus is within the waveguide). In the two-dimensional case, i.e. the slab waveguide, the input field distribution is proportional to

$$f(x') = \frac{\sin\left(\pi \dfrac{x'}{w}\right)}{x'} \tag{1}$$

i.e., a sinc distribution with the first zeros at $|x'| = w$. Thus the spot width of the input beam is $2w$. A tilt represented by the angle $\varepsilon \neq 0$ in the field distribution is expressed by using a slightly rotated coordinate system with x' instead of x. Since differences in the field distributions for the two possible polarization states TE (electric field polarized orthogonal to the plane of incidence) and TM (magnetic field polarized orthogonal to the plane of incidence) are rather small, we will, in the following, only consider the case of TE polarization, i.e. the input field is polarized along the y-direction.

In the three-dimensional case, i.e. the fiber waveguide, the incident radiation is again assumed to be focused by a lens. However, here we will only consider the case of normal incidence ($\varepsilon = 0$). The input distribution is thus proportional to

$$f(r) = \frac{J_1\left(1.22\pi \dfrac{r}{w}\right)}{r} \quad \text{with} \quad r = \sqrt{x^2 + y^2} \,, \tag{2}$$

i.e., an Airy distribution whose first zero is at $r = w$. In the fiber case, the quantity $2w$ denotes the spot diameter of the input beam. J_1 represents the Bessel function of the first kind, order one.

For the characterization of the usefulness of a single-mode waveguide as a modal filter we introduce the following three quantities:

2.1. Near-core power

The near-core power $p(z)$ represents the fraction P_{DC} of the total power in the waveguide that is found within a width D_C centered around the core, normalized to the input power P_{in}, i.e.

$$p(z) = \frac{P_{DC}(z)}{P_{in}} \tag{3}$$

D_C should be large enough to contain essentially all the power of the steady-state fundamental mode. Our choice of $D_C = 8a = 18\,\lambda_0$ provides more than 99.99% of the mode's power in P_{DC} for $z \to \infty$ for an operation at $\lambda = \lambda_0$. Even for a wavelength $\lambda = 1.5\,\lambda_0$, more than 99.3% of the power of the fundamental mode is included. Diagrams presenting the function $p(z)$ thus illustrate how fast the field in the waveguide approaches the fundamental mode.

In case of the fiber waveguide the calculation of power deserves special attention: Even if the plane wave incident on the lens is linearly polarized, say along the y-direction, as assumed for the numerical calculations, the field in the focal plane will also contain components – though small – in z and x direction, otherwise Maxwell's equations would not be satisfied. These components (E_z, E_x) are not Airy-distributed. The above defined quantities P_{DC}, P_{in} – and hence also $p(z)$ – contain all three field components. Along this line, the exact solution for the fundamental mode of a step index fiber does always contain all three field components [8], [9]. For the fiber parameters given in Table 1, the maximal E_z component is by a factor of 25 smaller than that of the dominating E_y component, and the maximum amplitude of E_x is smaller by another factor of 25. The numerical method we apply for calculating the field in the focal plane and in the fiber (see Section 3) does automatically yield the field components E_z and E_x.

2 2. Coupling efficiency

We define the coupling efficiency η as the ratio of the power carried by the waveguide's fundamental mode to the input power P_{in}. However, as the mode extends to infinity in transverse direction, the numerical determination requires a slightly modified definition. We maintain sufficient accuracy when taking – instead of the total power of the fundamental mode – the power P_{DC} for $D_C = 18\,\lambda_0$ in its limit for $z \to \infty$, designated $P_{DC,\,z \to \infty}$. The coupling efficiency is thus given as

$$\eta = \frac{P_{DC,z\to\infty}}{P_{in}} \tag{4}$$

2.3. Mode purity

So far we introduced quantities which characterize only the amount of light coupled into the fundamental mode. In contrast, the following definition of mode purity MP(L), with L as the waveguide length, offers a measure of how well the actual amplitude and phase distribution $E_w(x) = A_w(x)\exp(j\varphi_w(x))$ found just before the output pupil resemble the ideal distribution of the fundamental mode $E_f(x) = A_f(x)\exp(j\varphi_f)$. In case of the slab, the quantities E_w, A_w, φ_w and E_f, A_f, are functions of x, while for the fiber they depend on the coordinates r and φ. We define mode purity by means of output powers P_+ and P_-, as indicated in the right part of Fig. 1. The first one, P_+, is the power resulting from an in-phase superposition of the field E_w with the ideal field E_f, where for E_f we will take the numerical solution of the steady-state fundamental mode. The second one is due to an out-of-phase superposition. For determining P_+ and P_- we set – at the waveguide axis – the field amplitude A_f equal to A_w. In the same way, the phase relationship for calculating constructive and destructive interference, i.e. $\varphi_w - \varphi_f = 0°$ and $180°$, is defined at the waveguide axis. It turned out that the function MP(L) is almost independent on whether or not one includes the components E_z and E_x in the calculation of the three-dimensional case. To avoid unnecessary complexity, we based the calculation of mode purity MP of the fiber only on the amplitude and phase of the dominating y-components.

The powers P_+ and P_- depend on the pupil width D_B and are related to the corresponding field intensities I_+ and I_- by

$$P_{slab\pm} \propto \int_{-\frac{D_B}{2}}^{\frac{D_B}{2}} I_{slab\pm}(x)dx \quad \text{and} \quad P_{fiber\pm} \propto \int_{0}^{2\pi}\int_{0}^{\frac{D_B}{2}} I_{fiber\pm}(r,\varphi)rdrd\varphi \tag{5}$$

for the slab and the fiber, respectively. For the slab the intensities I_+ and I_- are in turn given by the electric fields as

$$I_{slab\pm} \propto \left| A_w(x,z=L)\exp[j\varphi_w(x,z=L)] \pm A_f(x)\frac{A_w(x=0)}{A_f(x=0)}\exp[j\varphi_w(x=0,z=L)]\right|^2, \tag{6}$$

and correspondingly for the fiber. The mode purity MP then follows as

$$MP = \frac{P_+}{P_-} \tag{7}$$

The quantity MP tends to infinity in the case where the field distribution E_w approaches that of the fundamental mode, E_f. In general, a smaller value of output pupil diameter D_B will result in a higher value of MP, however at the cost of reduced overall optical throughput.

3. Numerical method

To analyze the field distribution in the waveguide we employ a rigorous electromagnetic numerical tool that is based on the Fourier modal method (FMM) [7]. The FMM was originally developed in the field of grating theory. In recent years, however, a number of extensions and improvements added to the original idea have made FMM a versatile and popular tool dealing effectively with a much wider variety of micro-optical elements. A characteristic of FMM is that it requires the structure under investigation to be divided into segments with respect to the propagation direction, e.g., the z-direction. The thickness of each

segment is chosen such that the material parameters (e.g., the refractive index n) depend only on the transverse coordinates x and y. Within an individual segment the solution of Maxwell's equations can then be described in the form of

$$E(x, y, z) = S_m(x, y)e^{jb_m z} \qquad (8)$$

which defines the mth (eigen)mode for this specific segment. Mathematically, $S_m(x,y)$ and b_m represent the eigenfunction and eigenvalue of the solution. The simple harmonic z-dependence of the mode is the key to find solutions for long structures as efficiently as for short structures. The total field distribution in each segment is described via the complete basic set of modes which, in case of a waveguide structure, consists in general of a few guided modes and an infinite number of radiation modes. Fortunately, most of the higher-order radiation modes die off quickly with increasing propagation distance z and can therefore be neglected without sacrificing accuracy. For easy numerical handling, each mode is furthermore represented mathematically by a Fourier series. The x- and y-dependent material parameters are described by Fourier series as well. Each segment represents thus an autonomous eigenvalue problem whose solutions are the modal fields that are specific to the segment's geometry and material parameters. The complete set of modes in segment l is described by

$$E^l(x, z) = \sum_{m=-M}^{M} \left[\left(A_m^l \exp(jb_m^l z) + B_m^l \exp(-jb_m^l z) \right) \sum_{p=-P}^{P} \sum_{q=-Q}^{Q} S_{pqm}^l \exp(jKpx) \exp(jKqy) \right] \qquad (9)$$

where A_m^l and B_m^l stand for the mode amplitudes of forward and backward propagating waves, and $K = 2\pi/\Lambda$ is the fundamental spatial frequency with Λ being the structure's period in transverse direction. The 2M+1 eigenvectors summarized in S_{pqm} and the eigenvalues b_m represent now the complete set of solutions to the eigenvalue problem discussed above.

Apart from the focusing optics, the structure shown in Fig. 1 consists of three segments. A uniform semi-infinite input segment with a constant index n = 1, a thin metallic segment containing the x- and y-dependent index distribution of the input pupil, and a semi-infinite output segment with the x- and y-dependent index distribution of the waveguide. The output pupil is part of the idealized optical set-up to compute the mode purity and therefore not considered in the rigorous simulations. The input field distribution in a uniform segment, such as free space, is represented by a set of plane waves since plane waves are the modes of a uniform segment and the matrix S_{pqm} degenerates therefore to a unitary matrix. On the other hand, the field distribution inside the waveguide is represented by both guided and radiation modes which are specific to the waveguide structure. The values P and Q determine the maximum size of the Fourier representation. The magnitudes of M, P and Q affect the accuracy of the calculation but also the amount of computational time and dynamic memory and therefore need to be chosen carefully. Finally, by adjusting the mode amplitudes A_m^l and

B_m^l such that the field distributions fulfill Maxwell's boundary conditions at each segment interface, we obtain a system of linear equations that is solved numerically by matrix computation.

Although the use of Fourier series makes the system periodic in transverse direction, we are still able to analyze single aperiodic elements such as waveguides by introducing absorbing, perfectly matched layers along the rim of the calculation area parallel to the z-direction. The absorption and thickness of these layers must be chosen such that field contamination from neighboring waveguide structures due to the inherent periodicity is kept to a minimum. The condition of perfect matching with respect to the material parameters is needed for suppressing reflections from these additional layers [10].

4. Field behavior for various waveguide geometries and input coupling situations

In this section we present numerical results both for the slab and fiber single-mode waveguide:

First, two-dimensional color coded intensity distributions for various input coupling situations give a physical insight into how the incident free-space beam is either converted into the waveguide's fundamental mode or distributed across the cladding in form of radiation modes. In accordance with Fig. 1, the input radiation enters the waveguide from the left, passes through a transient region whose length mainly depends on the coupling situation, and eventually approaches the fundamental mode. To visualize the field behavior within a large dynamic range, the intensity distributions are normalized with respect to their maximum values and shown on a logarithmic scale from 0 to -40 dB. The waveguide's core region appears therefore as a red horizontal bar, as this is the location of highest intensity. In these figures we have indicated the waveguide input facet and the core-cladding boundaries by thin black vertical and horizontal lines.

Second, more quantitative information about coupling efficiency and power variation within a cross section of width $D_C = 18\,\lambda_0$ in core vicinity can be read off from graphs showing the near-core power p(z) along the z-direction.

Finally, the waveguide's filter quality is estimated with the help of graphs showing the mode purity MP as a function of waveguide length L.

4.1 The slab waveguide

Using the waveguide parameters specified in Section 2 for the slab waveguide, we found that *without* input pupil and for operation at $\lambda = \lambda_0$ the maximum coupling efficiency into the fundamental mode is obtained with an input beam width of close to $2w = 11\,\lambda_0$ and perfect alignment (see Fig. 2). This scenario will serve as a reference. Most of the power not guided by the waveguide is radiated off within the first $1000\,\lambda_0$ behind the input facet under an angle of approximately $\alpha = \pm 4°$. Figure 2(b) provides an in x-direction magnified version of Fig. 2(a), covering an area of $100\,\lambda_0$ x $4000\,\lambda_0$ of the waveguide (again with unequal scale in x- and z-direction) plus an area of $100\,\lambda_0$ x $100\,\lambda_0$ in front of the facet to illustrate the converging input beam.
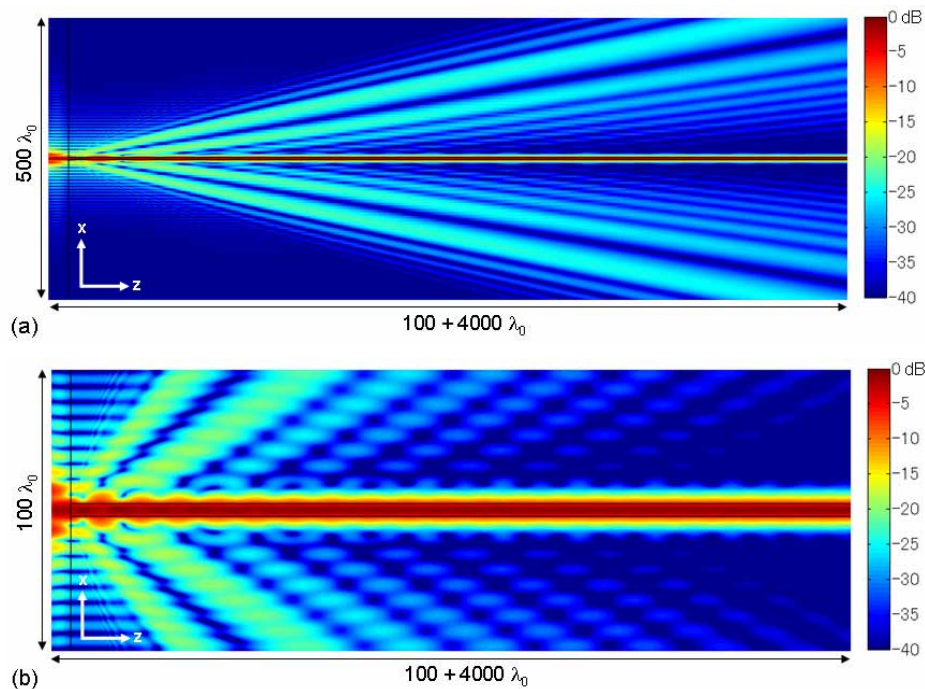
Fig. 2. Slab waveguide operated at $\lambda = \lambda_0$: Intensity distributions *without* input pupil for a beam width of $2w = 11\,\lambda_0$ and perfect alignment ($\Delta z = 0$, $\varepsilon = 0$, $\Delta x = 0$). (a) extension in x-direction is $500\,\lambda_0$, (b) extension in x-direction is $100\,\lambda_0$.

Next we investigated the effect of an input pupil on the field behavior in the transient region. We found that a pupil width of $D_A = 11\,\lambda_0$ exactly matching the beam width ($2w = 11\,\lambda_0$) leads to optimum coupling efficiency. Figure 3(a) depicts again the intensity distribution for perfect alignment, while Figs. 3(b) to 3(d) demonstrate the influence of input beam misalignments. In Fig. 3(b), a shift of the focal spot by $\Delta z = 50\,\lambda_0$ beyond the input facet results in an increased amount of power radiated off in a wider angular range. Figures 3(c) and 3(d) show how angular and lateral misalignment lead to enhanced power loss in the transient region. For an input angle of $\varepsilon = 1°$ we find an asymmetric radiation of the unguided modes, while close-to-symmetric behavior was observed for a lateral displacement of $\Delta x = 1\,\lambda_0$. Note that both misalignments cause a similar oscillatory behavior of the field around the waveguide axis, resulting in a significant extension of the transient region.

When comparing Figs. 2(b) and 3(a) it is evident that a pupil with a properly chosen width is capable of suppressing the radiation modes to some extent. We conclude that for waveguides without input pupil the number of radiation modes excited does not only increase with increasing mismatch between the sinc distribution's central lobe and the waveguide's fundamental mode but is also caused by the sinc distribution's sidelobes, half of which are out-of-phase with the main lobe
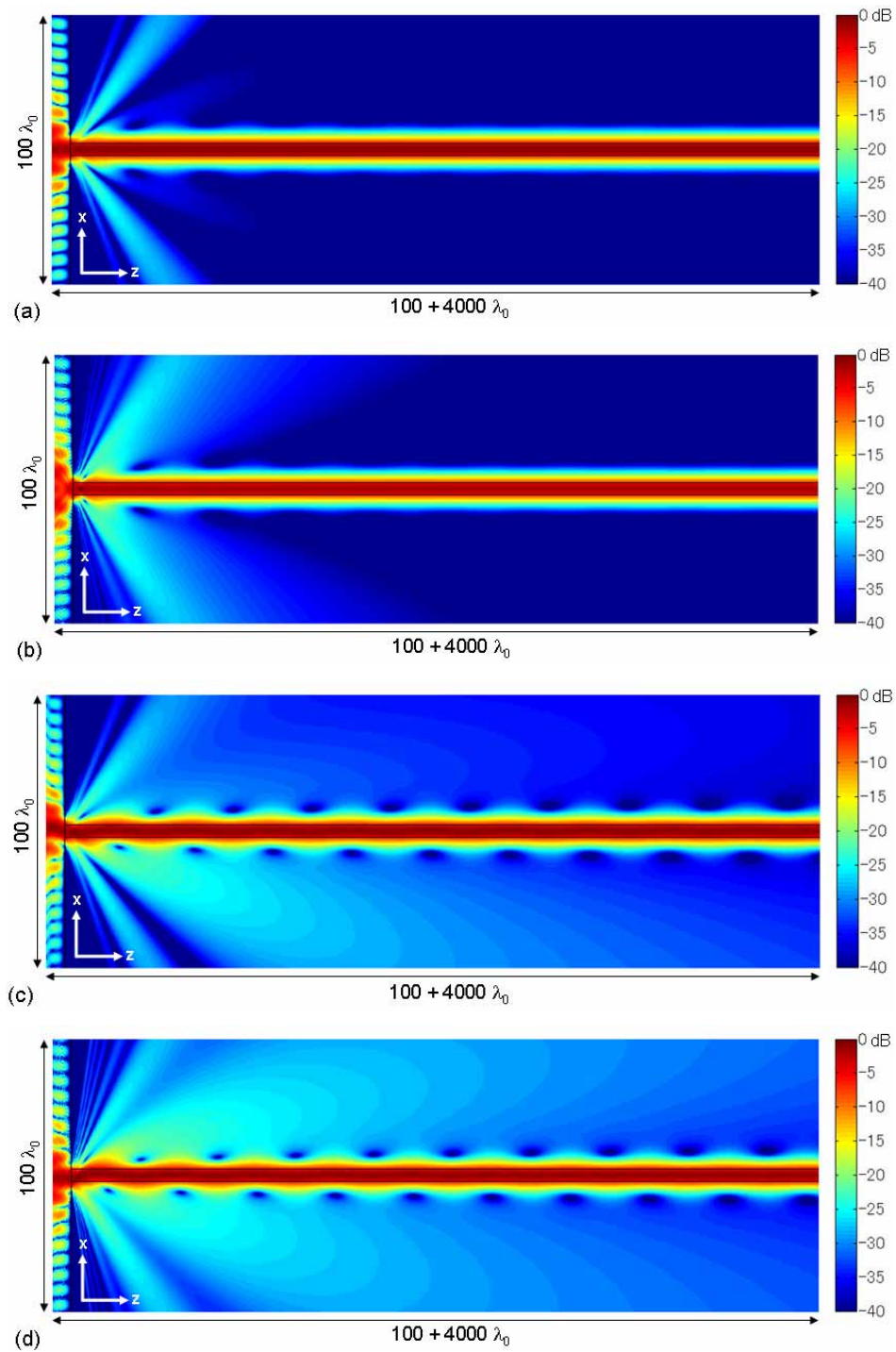
Fig. 3. Slab waveguide operated at $\lambda = \lambda_0$: Intensity distributions with input pupil ($D_A = 11\,\lambda_0$) for a beam width of $2w = 11\,\lambda_0$.   (a) perfect alignment ($\Delta z = 0$, $\varepsilon = 0$, $\Delta x = 0$) (b) defocus $\Delta z = 50\,\lambda_0$ (c) angular misalignment $\varepsilon = 1°$ (d) lateral misalignment $\Delta x = 1\,\lambda_0$.

Figure 4 shows how the near-core power p(z) gradually approaches the steady state for the five cases discussed above. The values on the right represent the coupling efficiencies η. In case of perfect alignment, these near-core power graphs confirm the positive effect of an input pupil in a twofold way: First, coupling efficiency is increased by some 2%, and second, the field approaches the steady state within a shorter distance.
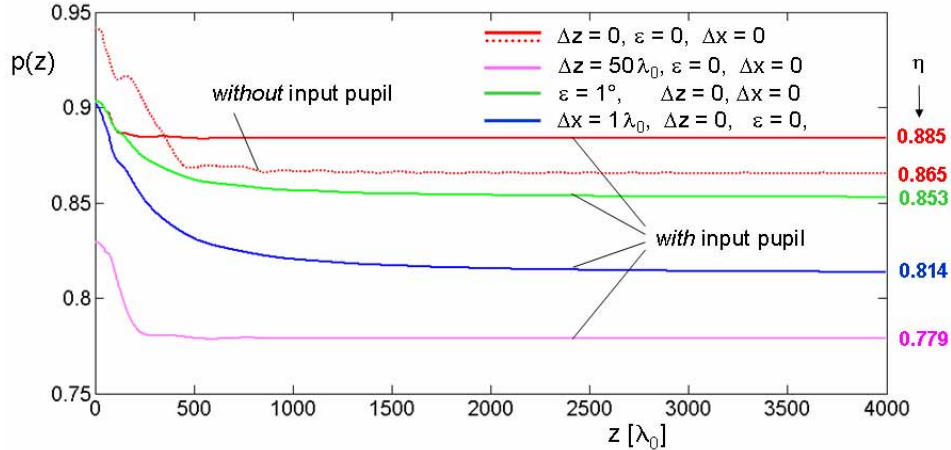
Fig. 4. Slab waveguide: Near-core power p(z) as a function of distance z from the input facet for the cases of Fig. 2 and Figs. 3(a) to 3(d). The numbers at the right give the coupling efficiencies η.

The presence of an input pupil also affects the mode purity MP in a favorable way. Figure 5 shows MP as a function of waveguide length L for two input pupil widths, namely for the optimized value of $D_A = 11 \lambda_0$ and for a much larger one with $D_A = 100 \lambda_0$. The latter is practically identical to the case without input pupil $D_A = \infty$. These graphs again demonstrate that the presence of sidelobes in the input beam keeps the field longer in its transient state and therefore requires a longer waveguide length to reach the same value of mode purity. In our specific example the waveguide without pupil would require about twice the length to achieve a mode purity of $MP = 10^7$.
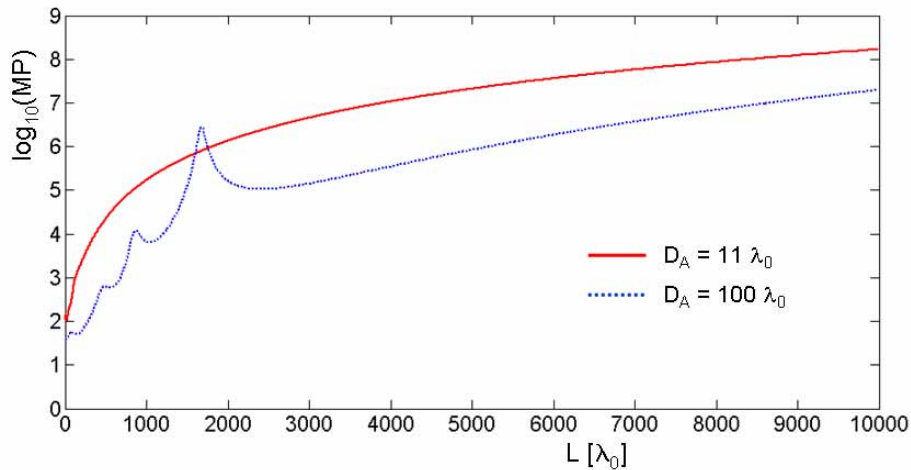

Fig. 5. Slab waveguide operated at $\lambda = \lambda_0$: Mode purity MP as a function of waveguide length L for a beam width of $2w = 11 \lambda_0$ and for input pupil diameters of $D_A = 11 \lambda_0$ and $D_A = 100 \lambda_0$. The latter case is practically identical to the case without input pupil ($D_A = \infty$).

In Fig. 6 we present mode purity graphs for the four cases of input coupling covered in Fig. 3 for two different wavelengths of the input radiation, i.e. for the design wavelength $\lambda = \lambda_0$ and for a wavelength increased by 50% ($\lambda = 1.5\,\lambda_0$). We assume the focusing optics to be one and the same and thus the beam width to increase by a factor of 1.5 when operating at $\lambda = 1.5\,\lambda_0$, i.e. $2w = 16.5\,\lambda_0$. While the mode purity is strongly affected by misalignments when operating the waveguide at the design wavelength (i.e. just below the waveguide's single mode cut-off frequency), these influences are less pronounced for operation at longer wavelengths. However, this comes at the cost of a reduced coupling efficiency η: For a fixed input width of $D_A = 11\,\lambda_0$ we found that η is reduced by 0.58 dB for operation at $\lambda = 1.5\,\lambda_0$.
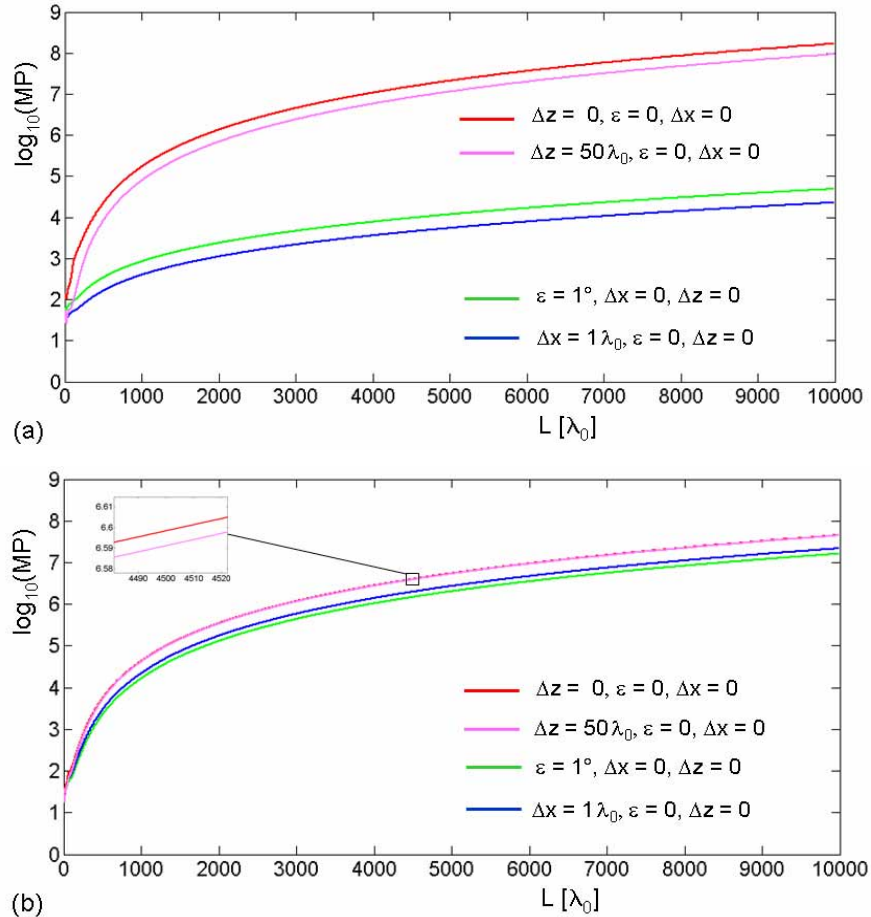

Fig. 6. Slab waveguide: Mode purity MP as a function of waveguide length L for the four cases of alignment specified in Fig. 3. (a) for operation at $\lambda = \lambda_0$, (b) for operation at $\lambda = 1.5\,\lambda_0$.

4.2. Field behavior of the slab waveguide with core inhomogeneities

Next we investigated the effect of small variations of the core diameter and core refractive index on mode purity and near-core power p(z). To this end, we divided the waveguide into three large sections. The first and third section consist of a homogeneous waveguide region equal the one discussed in Section 4.1. The middle section is subdivided into 400 small waveguide segments whose lengths vary randomly between $3\,\lambda_0$ and $7\,\lambda_0$. Furthermore, each segment contains a core whose refractive index varies randomly between 1.503 and 1.50375

and whose width varies randomly between $4\,\lambda_0$ and $4.5\,\lambda_0$ (see Fig. 7). The total length of the inhomogeneous section is approximately $2000\,\lambda_0$.
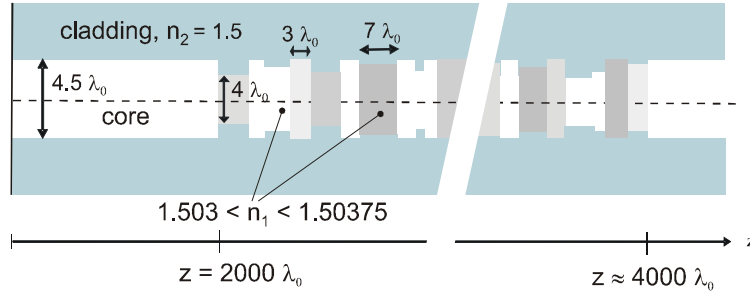

Fig. 7. Schematic of inhomogeneous waveguide.

The mode purity as shown in Fig. 8 was evaluated with respect to the fundamental mode in the homogeneous (first or third) region as a function of waveguide length L. Shortly after the onset of the inhomogeneous region the mode purity collapses to values below 10^4 and stays there as long as inhomogeneities are present. Recovery to higher values is only possible after the field enters again the homogeneous region.
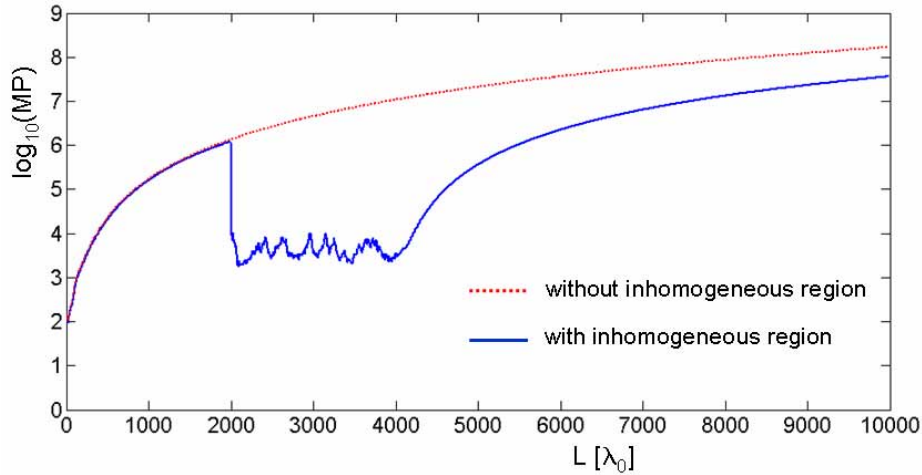

Fig. 8. Slab waveguide operated at $\lambda = \lambda_0$: Mode purity as a function of L for a waveguide *with* (blue) and *without* (red) an inhomogeneous core with a length of about $2000\,\lambda_0$, starting at $z = 2000\,\lambda_0$. The input beam parameters are $2w = 11\,\lambda_0$ and perfect alignment.

While the effect of inhomogeneities on the mode purity is quite dramatic, the loss in near-core power remains small (of the order of 1%), as shown in Fig. 9. Clearly, reflections from the inhomogeneous section ($2000\,\lambda_0 < z < 4000\,\lambda_0$) affect the field in the first homogeneous region ($0 < z < 2000\,\lambda_0$). The seemingly long period of some $200\,\lambda_0$ of the excited standing wave in this region is a numerical artifact caused by undersampling (one sample per $2\,\lambda_0$) of the function p(z) in direction of increasing distance z and cannot be directly related to the waveguide geometry or material parameters.
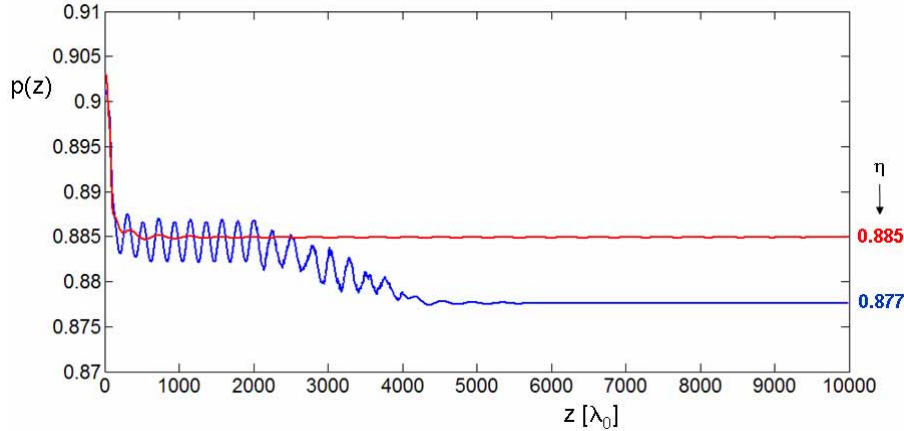
Fig. 9. Slab waveguide operated at $\lambda = \lambda_0$: Near-core power p(z) as a function of distance z for a waveguide *with* (blue) and *without* (red) inhomogeneities. The input beam parameters are $2w = 11\,\lambda_0$ and perfect alignment. The values at the right of the diagram represent the coupling efficiencies η to the fundamental mode in the third section.

4.3. Fiber waveguide

In a similar vein, as with the slab waveguide, we characterize the field in a fiber waveguide's transient region by calculating the two-dimensional intensity distributions in the plane containing the fiber axis z, the coupling efficiencies, the near-core power, and the mode purity. The definitions for these characteristics are the same as the ones given by Eqs. (4), (5) and (7) except that the power is now obtained by integrating over an axis-centered circular area of diameter D_C in case of near-core power and coupling efficiency, and diameter D_B in case of the mode purity. The huge requirements on dynamic memory and computation time for such three-dimensional simulations were partly relaxed by exploiting mirror symmetries [11] of the input field and the waveguide structure with respect to the transverse coordinates x and y. On the other hand, the use of such symmetries restricted our present study to on-axis input field illumination at normal incidence only, i.e. to $\varepsilon = 0$ and $\Delta x = 0$.

For the fiber parameters specified in Section 2, the maximum coupling efficiency into the fundamental mode of a waveguide *without* input pupil and operated at $\lambda = \lambda_0$ is obtained for an input beam diameter close to $2w = 8.8\,\lambda_0$. The corresponding intensity distribution is shown in Fig. 10. Similar to the case of the slab waveguide, the mismatch between the incident Airy distribution and the distribution of the fundamental mode gives rise to several radiation modes which spread into the cladding, with cone angles of up to some 5°. Obviously, for wave propagation in three dimensions, these radiation modes die off much faster than their two-dimensional counterparts, thus reducing the length of the transient region compared to the slab guide. As expected, if the input matching is reduced by defocusing [see Fig. 10(b)], more power is radiated off into the cladding.
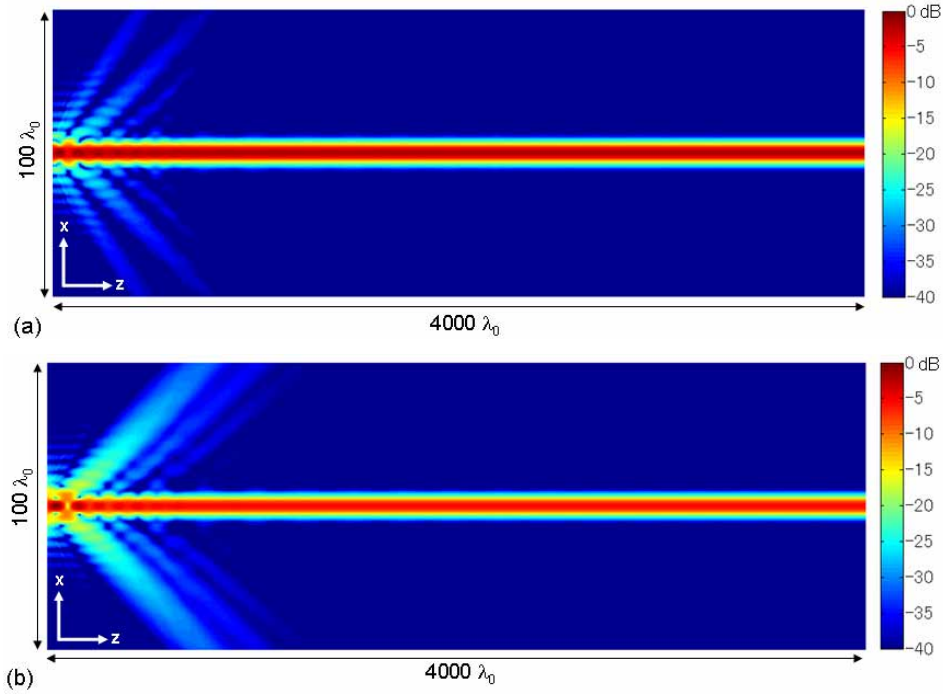
Fig. 10. Fiber operated at $\lambda = \lambda_0$: Intensity distributions *without* input pupil, input beam diameter $2w = 8.8\ \lambda_0$. (a) perfect alignment
(b) defocus $\Delta z = 50\ \lambda_0$.

As with the slab waveguide, we expect also for the fiber to find an improvement of the transient field by placing a (circular) pupil in front of the waveguide's input facet. Figure 11 demonstrates that an input pupil which is matched to the input beam diameter significantly reduces both the amount of radiated power into the cladding and the length of the transient region. Here, too, defocusing will result in both suboptimal amplitude and phase distribution at the input and thus increases the amount of power going into the radiation modes, as evidenced by Fig. 11(b).
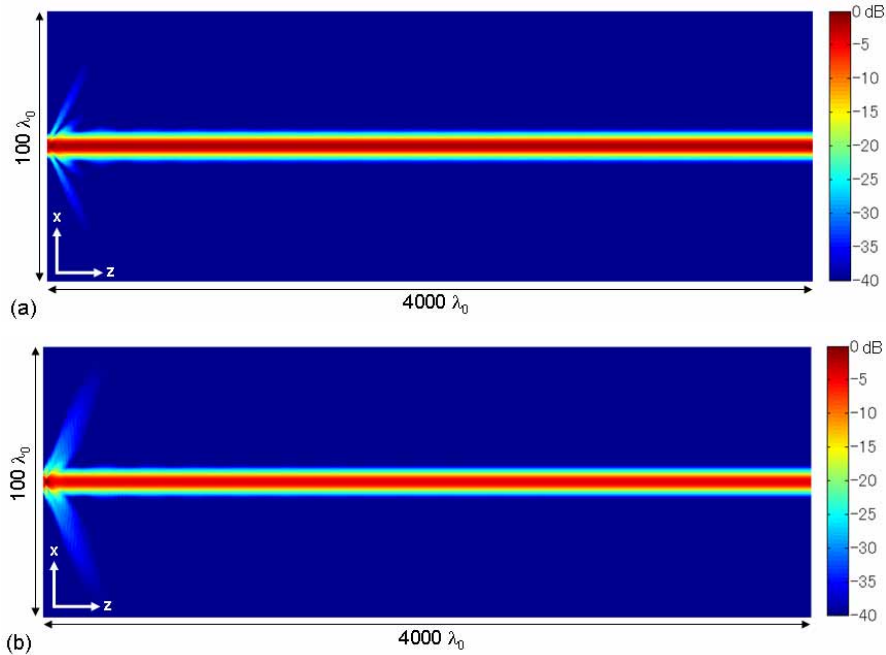
Fig. 11. Fiber operated at $\lambda = \lambda_0$: Intensity distributions *with* input pupil, input beam diameter $2w = 8.8\ \lambda_0$. (a) perfect alignment
(b) defocus $\Delta z = 50\ \lambda_0$.

The near-core power p(z) for both cases is shown in Fig. 12. Whether with or without misalignment, the power converges quickly, i.e. within the first $200\ \lambda_0$, towards the value suggested by the coupling efficiency. The curves also confirm the positive effect of the input pupil on the coupling efficiency, whose improvement amounts to nearly 3% in this specific example.
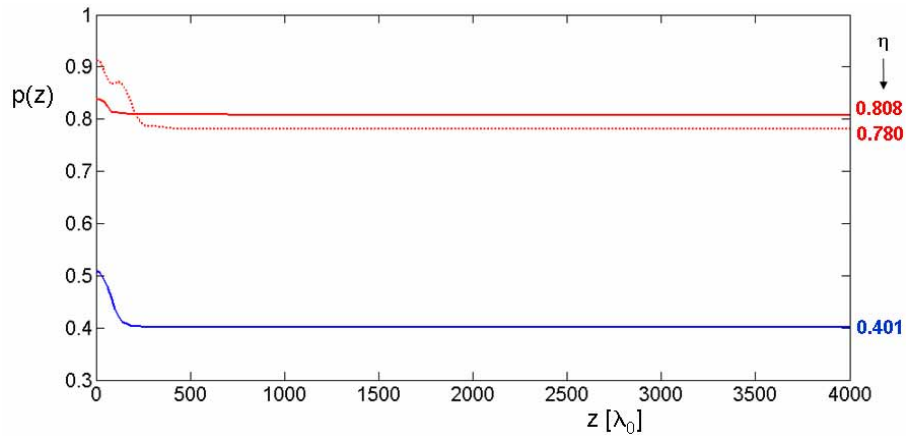

Fig. 12. Fiber operated at $\lambda = \lambda_0$: Near-core power p(z) as a function of distance z for $2w = 8.8\ \lambda_0$. The numbers at the right give the coupling efficiencies η. Dotted red line: perfect alignment without input pupil $(D_A = \infty)$ Solid red line: perfect alignment with input pupil $(D_A = 8.8\ \lambda_0)$ Blue line:defocus $\Delta z = 50\ \lambda_0$, with input pupil $(D_A = 8.8\ \lambda_0)$.

Finally, the dependence of mode purity MP on fiber length L is shown in Fig. 13 and Fig. 14. Figure 13 compares the mode purity for input pupils that strongly differ in their

diameter. Similar to the slab waveguide, the presence of an input pupil increases the mode purity by an order of magnitude for a given fiber length. Figure 14 shows two pairs of MP curves for the cases of two different input coupling conditions (*with* and *without* a focal shift of $\Delta z = 50\,\lambda_0$) and two different wavelengths. The curves for the longer wavelengths are less affected by misalignment, however the coupling efficiency is reduced by some 1.7 dB due to the larger input beam size and the fixed input pupil diameter. As with the slab waveguide, the increase of wavelength by a factor of 1.5 entails a larger spot size, i.e. $2w = 13.2\,\lambda_0$.
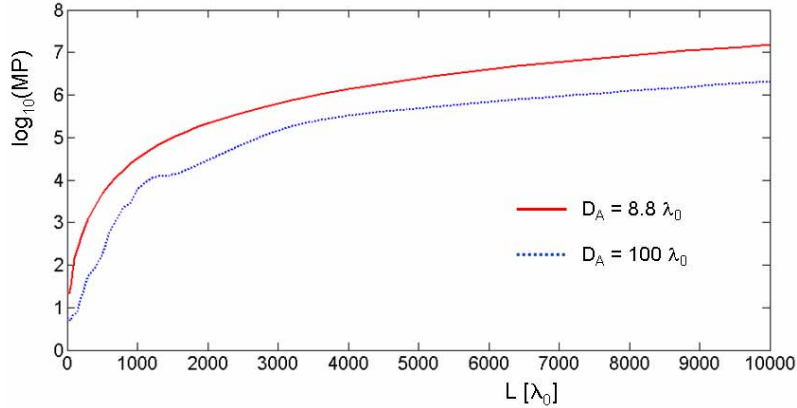

Fig. 13. Fiber operated at $\lambda = \lambda_0$ with input beam diameter $2w = 8.8\,\lambda_0$: Mode purity MP as a function of waveguide length L for input pupil diameters of $D_A = 8.8\,\lambda_0$ and $D_A = 100\,\lambda_0$. The latter case is practically identical to the case without input pupil ($D_A = \infty$).
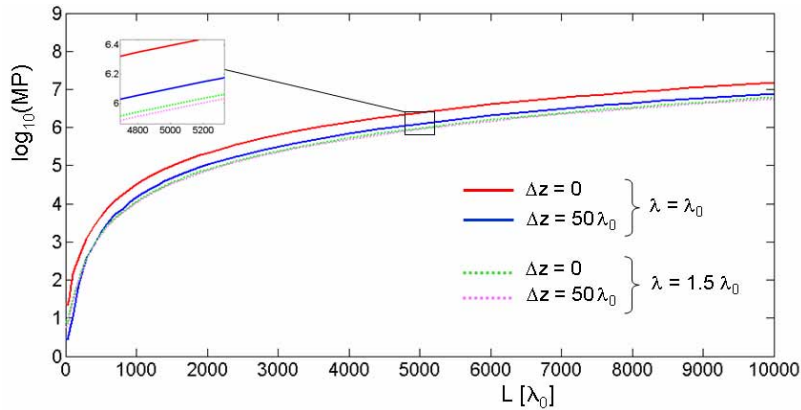

Fig. 14. Fiber: Mode purity MP as a function of waveguide length L for perfect alignment (red line) and for a defocus of $\Delta z = 50\,\lambda_0$ (blue line) when operated at $\lambda = \lambda_0$. The dotted lines give MP for operation at $\lambda = 1.5\,\lambda_0$ (green line: perfect alignment, magenta line: defocus of $\Delta z = 50\,\lambda_0$).

5. Comparison of fields in slab and fiber waveguide

Figure 15 compares the near-core power p(z) for the slab waveguide (dotted lines) and the fiber waveguide (solid lines) for normal incidence and an input pupil width equal to the beam width ($D_A = 2w = 11\,\lambda_0$ for the slab, $D_A = 2w = 8.8\,\lambda_0$ for the fiber). The red lines represent perfect alignment, the blue lines a defocus of $\Delta z = 50\,\lambda_0$. The near-core power for the fiber waveguide shows a slightly faster convergence towards the coupling efficiency value. This may be attributed to the fact that here unguided radiation is distributed over the total waveguide volume, i.e. in three-dimensional space, while for the slab geometry it is

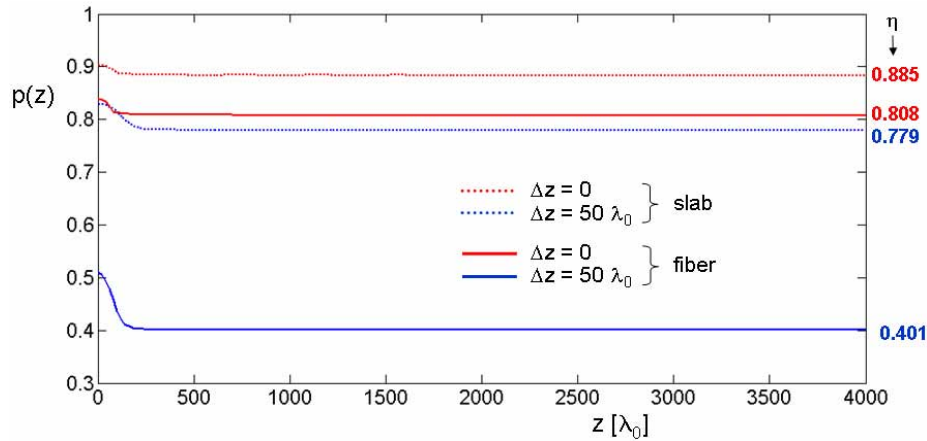distributed only over the x-z plane. As expected, defocusing causes smaller coupling efficiency η.

Fig. 15. Comparison of near-core power p(z) for slab (dotted lines) and fiber (solid lines) *with* input pupils, operated at $\lambda = \lambda_0$. The red lines are for perfect alignment, the blue lines for a defocus of $\Delta z = 50 \lambda_0$.

In Fig. 16 we compare mode purity MP as a function of waveguide length L for the slab waveguide and the fiber waveguide. Again, both cases are evaluated for a system with input pupil widths equal to the optimum beam widths. The output aperture width was taken as $D_B = 18 \lambda_0$. As expected, for given length L perfectly aligned input fields (red lines) lead to higher mode purity than slightly defocused fields (blue lines). To achieve the same value of mode purity, the fiber waveguide (solid lines) requires a longer length. This behavior may be attributed to the different integration areas in the two-dimensional and three-dimensional case when determining the power values P_+ and P_-.
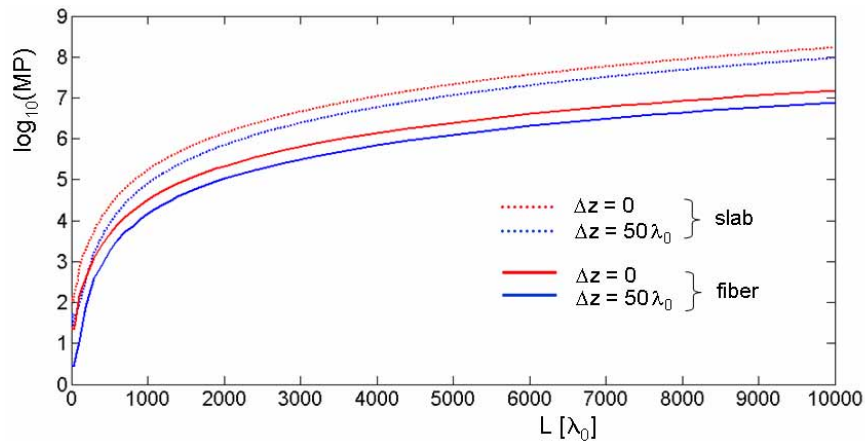

Fig. 16. Comparison of mode purity MP for slab (dotted lines) and fiber (solid lines) *with* input pupils, operated at $\lambda = \lambda_0$. The red lines are for perfect alignment, the blue lines for a defocus of $\Delta z = 50 \lambda_0$.

6. Comparison of numerical results and analytical solutions

In case of perfect alignment of the input field we can compare some of the results obtained by the numerical field calculation with analytical solutions. This comparison also serves as validity check for our numerical results where analytical solutions are not available. As demonstrated in Table 2, except for two out of the 16 cases, excellent agreement is obtained, giving a clear indication of the correctness of our numerical approach. For the two cases, highlighted in grey, we explain the difference as follows: Due to the larger focal spot size, the incident field shows at the metallic pupil a non-zero tangential field component in case of the slab waveguide and non-zero tangential and normal field components in case of the fiber waveguide. This causes some absorption and field distortion by the pupil which changes the field shape at $z = 0$ (the location of the waveguide's facet) and therefore also affects the coupling efficiency η. Of course this effect could not be taken care of in the analytical calculation. Note that in the fiber case the numerical results took into account all three field components E_x, E_y and E_z, while the analytical results are based on the assumption of the existence of the single field component E_y only.

Table 2: Comparison of results (perfect alignment).

waveguide	wavelength λ	item	numerical result	analytical result
slab	λ_0	p(z = 0) for $D_A = \infty$ (no input pupil) [2]	0.942	0.9417
		p(z = 0) for $D_A = 11\,\lambda_0$	0.903	0.9028
		coupling efficiency η for $D_A = \infty$	0.865	0.8652 [1]
		coupling efficiency η for $D_A = 11\,\lambda_0$	0.885	0.8849 [1]
	$1.5\,\lambda_0$	p(z = 0) for $D_A = \infty$ [2]	0.903	0.9033
		p(z = 0) for $D_A = 11\,\lambda_0$	0.865	0.8675
		coupling efficiency η for $D_A = \infty$	0.842	0.8419 [1]
		coupling efficiency η for $D_A = 11\,\lambda_0$	0.785	0.8049 [1]
fiber	λ_0	p(z = 0) for $D_A = \infty$ [2]	0.913	0.9135
		p(z = 0) for $D_A = 8.8\,\lambda_0$	0.838	0,8378
		coupling efficiency η for $D_A = \infty$	0.780	0.7802 [1]
		coupling efficiency η for $D_A = 8.8\,\lambda_0$	0.810	0.8124 [1]
	$1.5\,\lambda_0$	p(z = 0) for $D_A = \infty$ [2]	0.872	0.8712
		p(z = 0) for $D_A = 8.8\,\lambda_0$	0.759	0.7609
		coupling efficiency η for $D_A = \infty$	0.717	0.717 [1]
		coupling efficiency η for $D_A = 8.8\,\lambda_0$	0.609	0.643 [1]

1) including truncation by output aperture of width $D_B = 18\,\lambda_0$
2) here truncation is due to the definition of "near-core power", i.e. by the width D_C

7. Summary and conclusion

When the field at the input facet of a single-mode waveguide does not perfectly match the one of the waveguide's fundamental mode, the actual formation of the fundamental mode is a process which may take place over a length of few hundreds to a few thousands of wavelengths. Using the Fourier Modal Method we have calculated the transient fields after the input facets of both slab and fiber step-index waveguides. While color-coded diagrams

showing the intensity distribution in the meridional plane give a good qualitative picture of how the unguided power is radiated off, the near-core power is a quantitative measure of the development of the fundamental mode along the waveguide axis. Lastly, our definition of mode purity allows us to determine to a very high degree the identity of the actual waveguide field with the ideal mode. In this context, the definition of an exit pupil turned out to be essential.

For the numerically evaluated examples we have assumed parameters leading to a fundamental mode with a normalized frequency a few percent below the next mode's cut-off. We showed that the establishment of the fundamental mode strongly depends on both the distribution of the input field and any misalignment of the input wave. Mode purity is very sensitive to even small misalignments of input field and to any variations in waveguide geometry. For the typical input field distribution containing side lobes, the placement of a pupil just in front of the waveguide's facet is advantageous when striving for single-mode purity in short waveguide lengths. Such a pupil could be realized by evaporating a metal film onto the input facet of the slab waveguide or fiber. The pupil helps to remove unwanted field components from the input field that may interfere with the fundamental mode. It also somewhat relaxes the dependence of mode purity on misalignments. However, it lowers the coupling efficiency for larger wavelengths in a broadband application.

The treatment of the three-dimensional case (i.e. the fiber) is computationally much more extensive than that of the two-dimensional case (i.e. the slab). However, we found that fiber waveguides do not exhibit significantly different behavior in the characteristics of near-core power and mode purity when compared to their two-dimensional counterparts. Thus an insight into the performance of the fiber can indeed be obtained by first studying the equivalent slab problem.